The analysis of using satellite soil moisture observations for flood detection, evaluating over the Thailand's Great Flood of 2011

Natthachet Tangdamrongsub [1,2], Chalita Forgotson [3,2], Chandana Gangodagamage [1,2], Joshua Forgotson [4]

[1] Earth System Science Interdisciplinary Center, University of Maryland, College Park, Maryland, USA

[2] Hydrological Sciences Laboratory, NASA Goddard Space Flight Center, Greenbelt, Maryland, USA

[3] Science Applications International Corporation, Lanham, Maryland, USA

[4] ICF, Fairfax, VA, USA

Correspondence to: natthachet.tangdamrongsub@nasa.gov

Abstract

A flood monitoring and warning system provides critical information that can protect property and save lives. A basin-scale flood monitoring system requires an effective observation platform that offers extensive ground coverage of flood conditions, low latency, and high spatiotemporal resolution. While satellite imagery offers substantial spatial flood extent in detail due to its high spatial resolution, the coarse temporal resolution and cloud obstruction limit its near real-time application. Daily soil moisture data derived from satellite sensors at a scale of a few km can be used to monitor extreme wet surface conditions arising in flood occurrences. This study analyses the flood detection capabilities of several sources of soil moisture information, including the Soil Moisture and Ocean Salinity mission (SMOS), the Advanced Microwave Scanning Radiometer on EOS (AMSR-E), the Advanced SCATterometer (ASCAT) on MetOp, the Global Land Data Assimilation System (GLDAS), and the WaterGAP Global Hydrology Model (WGHM). In addition to soil moisture, the analysis includes measurements of surface reflectance from the Moderate Resolution Imaging Spectroradiometer (MODIS), precipitation measurements from the Tropical Rainfall Measuring Mission (TRMM), and terrestrial water storage estimates from the Gravity Recovery And Climate Experiment (GRACE) as proxies for flood inundations. The analysis was conducted over the Chao Phraya River Basin (CPB) in Thailand, where the Great Flood of 2011 led to one of the most significant economic losses in the country's history. Satellite-derived soil moisture exhibits a stronger correlation with the flood inundations than the precipitation, model-derived soil moisture, and terrestrial water storage data. SMOS soil moisture observation agrees best with the MODIS-derived flood extent/occurrence, both in terms of spatial distribution and timing, and providing approximated flood lead-time of one week or longer. A neural network constructed from SMOS and MODIS data is used to predict flood intensity/occurrence (given soil moisture input) with a predicted time window from eight days to thirty-two days. The short-term prediction (e.g., eight days) achieves the highest accuracy with an averaged recovery rate of approximately 60% (correlation coefficient). This study's results suggest a potential application of satellite soil moisture data in assisting flood monitoring and warning systems.

Keywords: Satellite soil moisture; SMOS; MODIS; Flood prediction; Thailand’s Great Flood

1. Introduction

Observation networks of natural disasters across ground and space domains have become more important given climate intensification, which likely leads to ever more extreme events (Mirza 2003; Lebel et al. 2011; Coumou and Rahmstorf 2012; Hirabayashi et al. 2013). Such information is vital for decision making to mitigate the casualties and economic loss of natural disasters (Shook 1997; Few 2003; Lin Moe and Pathranarakul 2006). The global and continental-scale flood monitoring, modeling, and prediction systems have shown a fast-growing development during the last decades. Many sophisticated tools have been developed to accurately forecast the dynamics of flooding (Adams and Pagaon 2016). However, due to the scarcity of adequate observations and modeling systems, this technological advancement did not benefit ungauged flood-prone areas in developing countries or data-sparse regions (Sanyal et al. 2013; Komi et al. 2017). Satellite data can potentially address this shortcoming by providing rapid, efficient, and accurate surface water mapping and flooded inundation areas. Due to its temporal and spatial coverage capacity, remote sensing has emerged as a powerful tool for mapping inundation.

Optical measurements, e.g., satellite imagery, are commonly employed in monitoring or analysis of floods because of their high spatial resolution and coverage, providing basin-scale measurements at a resolution of as fine as a few meters (e.g., Smith 1997; Khan et al. 2011; Ahamed and Bolten 2017). The drawbacks of optical measurements include cloud obstruction, vegetation cover, and coarse temporal resolution, e.g., eight days, which in turn limit its application for monitoring near-real-time events. Satellite-based rainfall measurements have been considered as a potential component of flood monitoring systems (e.g., Toth et al. 2000; Hossain and Anagnostou 2004; Wu et al. 2014). However, multiple studies report high uncertainty of the measurement with regards to the success rate in the detection of extreme events (e.g., Mei et al. 2014; Maggioni et al. 2016; Bajracharya et al. 2017). Meanwhile, the consideration of soil moisture in the data assimilation system or neural networks has been adopted in some instances for streamflow and flood prediction (e.g., Anctil et al. 2008; Wanders et al. 2014; Alvarez-Garreton et al. 2014).

Soil moisture is a crucial variable in water-energy exchange between the land surface and atmosphere (Koster et al. 2004). Two major soil moisture components are surface soil moisture, e.g., the top 10 cm of soil, and root zone soil moisture, e.g., the top 200 cm. Both components play vital roles in climate variability and numerous geophysical events, including flooding (e.g., Eltahir 1998; Koster et al. 2004; Ray and Jacobs 2007; Tramblay et al. 2010). Soil moisture correlates with precipitation and runoff because it controls the partition of the water cycle components, i.e., the transition between rainfall and infiltration and between rainfall and surface runoff depends on the saturation of the soil. As such, soil moisture retains a memory of a few days to months (Koster and Suarez 2001). Such information was found to be useful for quantifying flood lead-time in various flood monitoring systems (e.g., Massari et al. 2014; Wanders et al. 2014).

Regional soil moisture information can be obtained from different satellite observations and numerical models, e.g., land surface models (Pitman 2003; Karthikeyan et al. 2017). Satellite soil moisture observations can retrieve surface soil moisture information at a depth of 1 – 5 cm and a spatial resolution of a few km (e.g., 25 km). Multiple satellite soil moisture observatories have been operated over the last decade, including the Advanced Microwave

Scanning Radiometer onboard NASA's Earth Observation Satellite Aqua (AMSR-E, Njoku et al. 2005), the Advanced SCATterometer (ASCAT) onboard the Meteorological Operational satellite (Wagner et al. 1999), the Soil Moisture and Ocean Salinity mission (SMOS; Kerr et al. 2012), the Soil Moisture Active Passive mission (SMAP; Entekhabi et al. 2010), and the Synthetic Aperture Radar (CSAR) sensors of the Sentinel-1 satellite (Bauer-Marschallinger et al. 2019). Daily satellite soil moisture observations from these observatories are insensitive to cloud interference and have a revisit period of approximately three days, which offers improved temporal resolution over the satellite imagery.

Soil moisture information can also be obtained from measurements of the Gravity Recovery And Climate Experiment (GRACE) satellite mission (Tapley et al. 2004). In contrast to measuring the surface soil layer, GRACE data provides measurements of the integrated water column (e.g., the sum of surface and root zone soil moisture, snow, groundwater, surface water, and canopy interception). Such information has been found valuable for a wide range of hydrological analyses (e.g., Long et al. 2014; Zhou et al. 2018; Gouweleeuw et al. 2018). A key limitation of GRACE is its coarse spatiotemporal resolution, i.e., 300 km and one month, and its restricted application, i.e., only to regions where the monthly water storage variation is significant (e.g., Longuevergne et al. 2013; Han et al. 2017; Farahani et al. 2017).

Alternatively, a land surface or hydrology model can be used to simulate the comprehensive soil moisture components at a desired spatiotemporal scale. A model is built upon complex physics to achieve a realistic representation of land-atmosphere interactions and hydrological cycle processes. It has been successfully applied in numerous flood studies (e.g., Long et al. 2014; Jung and Jasinski 2015; Zhou et al. 2018). This study employs soil moisture storage from the Global Land Data Assimilation System (GLDAS; Rodell et al. 2004) and the WaterGAP Global Hydrology Model (WGHM; Müller Schmied 2017) to assess the performance of numerical models for flood detection. The model comparison also provides insight into differences between the model configurations and physical processes considered, e.g., the inclusion of surface water and anthropogenic factors.

Information on precipitation and flood intensity/extension needed for flood detection analysis can be derived from data from the Tropical Rainfall Measuring Mission (TRMM; Huffman et al. 2007) and the Moderate Resolution Imaging Spectroradiometer (MODIS) (Vermote et al. 2015), respectively. In addition to the flood detection analysis, this study also makes predictions of flood intensity/occurrence from satellite soil moisture data, using a neural network constructed between satellite soil moisture and MODIS data. While a similar approach has been adopted with in situ observations (e.g., Anctil et al. 2008; Cruz et al. 2018), this study, for the first time, makes predictions of basin-scale flood intensity/occurrence based on satellite soil moisture data.

This study aims to analyze the sensitivity of different satellite soil moisture observations, compared to that of precipitation and terrestrial water storage observations, for flood detection. Particularly, the study's objectives lie in the following aspects, 1) to examine the strengths and weaknesses of various satellite observations for flood detection, 2) to benchmark the ability of satellite soil moisture data to capture flood events in both spatial and temporal domains, and 3) to quantify the accuracy of flood predictions derived from soil moisture data, including the effective predicted time window. The analysis is demonstrated over the Chao Phraya River Basin (CPB) in central Thailand, where the Great Flood of 2011

caused catastrophic loss of life and economic impacts. Results from this study may help improve flood monitoring systems in the CPB or other data-sparse regions with similar land surface characteristics.

2. Study region

The Chao Phraya River Basin (CPB) is a major river basin of Thailand, stretching about 600 km from northern to central provinces (Fig. 1). The region encompasses over ten major cities (including Bangkok, the capital city of Thailand) and five major rivers (Ping, Nan, Chao Phraya, Yom, Wang), and accommodates most of the country's cultivated land and fisheries. The CPB consists of three parts, northern, central, and southern. The northern CPB lies in mountainous regions with elevations greater than 2000 m, while the central and southern CPB accommodate the lowland Central Plain of Thailand (Mikhailov and Nikitina 2009). The region has a tropical climate with an average annual precipitation of ~1200 mm, where 90% of the rainfall is observed during the rainy season (e.g., May – October; Mikhailov and Nikitina 2009; Kure and Tebakari 2012). The region has been known to experience several episodes of extreme monsoon rainfalls, leading to multiple episodes of floods (Jamrussri and Toda, 2017). Three severe flood events were observed between 2000 and 2015, where the most severe flood event in 2011, known as the Great Flood of 2011, extended over 18,000 km^2 (see, e.g., Fig. 1b and 1c), causing the loss of almost USD 10 billion and 700 deaths (World Bank 2012). These significant losses have motivated multiple comprehensive studies to monitor, forecast, and assess the potential for future natural disasters using measurements across ground and space platforms, e.g., imagery, precipitation, and streamflow observations (e.g., Rakwatin et al. 2013; Bidorn et al. 2015; Pumchawsaun 2018). In addition to measurements used in previous studies, this study also includes the satellite soil moisture in the flood analysis and demonstrates its application to support flood monitoring and prediction.

[Suggested location of Figure 1]

3. Data processing

3.1 Satellite soil moisture retrievals

Surface soil moisture data are obtained from three different satellite products, SMOS, AMSR-E, and ASCAT (Table 1). These datasets are selected based on their data availability during our evaluation period (2002 – 2015). The SMOS's soil moisture retrieval is obtained from the Level 3 (release 4) daily product from the Centre Aval de Traitement des Données SMOS (CATDS, 2016; https://www.catds.fr, last access: 15 March 2020) operated for the Centre National d'Etudes Spatiales (CNES) by the French Research Institute for Exploitation of the Sea (IFREMER). The SMOS satellite uses the Microwave Imaging Radiometer with Aperture Synthesis (MIRAS) instrument to measure the multi-angular dual-polarisation brightness temperature of the Earth's surface. The MIRAS sensor is operated in L-band frequency (1.4 GHz), which is sensitive to soil moisture to a depth of 5 cm. The retrieval algorithm optimizes the fit between the brightness temperature observation and associated surface parameters used to derive the soil moisture (Bitar et al. 2017). The SMOS product

consists of reanalysis data from 2010 to 2014 and operational data from 2015 to the present (last access: 15 March 2020). The retrievals are provided in volumetric soil moisture content (m^3/m^3), with a spatial resolution of 25 km Equal-Area Scalable Earth (EASE, Brodzik et al. 2012) grid.

AMSR-E's soil moisture data is obtained from the Level 3 product of the VUA-NASA Land Parameter Retrieval Model (Owe et al. 2008). The AMSR-E sensor is a 6-band frequency radiometer (from 6.9 to 89 GHz) operating onboard the NASA EOS Aqua satellite. Like SMOS, the passive microwave sensor measures the brightness temperature of the dual-polarization, which is passed into a radiative transfer model to derive the soil moisture. The AMSR-E product provides a daily volumetric water content (%) of the top soil layer at 0.25°×0.25° spatial resolution between June 2002 and October 2011. The C-band (6.9 GHz) measurement is used in this study due to a deeper sensible soil depth (~2 cm).

ASCAT's soil moisture retrieval is obtained from the European Organisation for the Exploitation of Meteorological Satellite Application Facility on Support to Operational Hydrology and Water Management (EUMETSAT H-SAF) product (EUMETSAT H-SAF, 2007; http://hsaf.meteoam.it/soil-moisture.php; last access: 17 May 2020). The H109 product is used for this study's temporal coverage (2007 – 2015). The ASCAT is a C-band scatterometer (5.255 GHz) onboard the EUMETSAT Meteorological Operational Platforms (MetOp) satellite. The active radar sensor measures the backscattering coefficients, a function of soil moisture saturation, i.e., from 0% for dry soil to 100% for saturated wet soil. The derived soil moisture values reflect the wetness of the top 2 cm soil layer. The H109 product provides a near-daily gridded measure of soil moisture in terms of a degree of saturation (%) at 12.5 km sampling grid space.

The analysis performed for this paper focuses only on soil moisture anomalies. Therefore, the conversion between soil saturation and volumetric terms is not performed. For all three soil moisture products, the ascending and descending measurements are averaged when overlapped on the same day to reconcile with our analysis's time step (daily).

3.2 MODIS-derived flood intensity

Flood extent is derived using surface reflectance measurements from MODIS sensors onboard NASA's Aqua satellites. The MODIS Surface-Reflectance Product (MYD09A1, Vermote et al. 2015) provides the surface reflectance in 7 different frequency bands within an 8-day window at 500 m spatial resolution. The combinations of specific frequency bands can be used to identify open water bodies of the size of approximately ≥ 0.25 km^2. In this study, the multi-frequency surface reflectance is extracted from the MODIS tiles h2707 and h28v07 (covering the entire study area) between 2002 and 2015. The pixels flagged with severe cloud cover or fill values are masked based on data quality control flags provided with the MODIS product. The surface water extent is derived based on the normalized difference water index (NDWI) computed using the reflectance from green and near-infrared (NIR) channels as follows (McFeeters 1996):

$$NDWI = (green - NIR)/(green + NIR). \quad (1)$$

The NDWI ranges between -1 and 1, where the positive value represents open water, and the zero or negative values represent soil or vegetation canopy. The flooded area is computed by

multiplying the total number of open water pixels by 0.25 km^2 (the spatial resolution of the surface reflectance dataset).

3.3 GRACE-derived terrestrial water storage variation

Satellite soil moisture observation might fail to detect water storage variations associated with deeper soil layers than the satellite sensor can sense. By contrast, terrestrial water storage (TWS) observation reflects an integration of all water storage components, which may potentially capture the saturated soil condition more effectively. This study obtained TWS information from GRACE measurement. GRACE is a twin satellite-to-satellite tracking system measuring the change of Earth's gravity field based on various instruments, e.g., K-band ranging system, accelerometer, and global positioning satellite antennae (Tapley et al. 2004). The measurement can be used to represent the change of integrated water column (e.g., soil moisture, groundwater, snow, and surface water) at a monthly time scale. This study uses the monthly land-gridded product provided by the GRACE Tellus (https://grace.jpl.nasa.gov) between 2002 and 2015. The GRACE Tellus product is derived from the release-6 spherical harmonic solution of the Center for Space Research (CSR) at the University of Texas at Austin. The landmass is provided in terms of monthly 1°×1° globally gridded terrestrial water storage variation (ΔTWS), representing the equivalent water thickness change of the unit area (1°×1° pixel). After obtaining GRACE data, the long-term mean computed by averaging all monthly data between 2002 and 2015 is removed from the monthly data to obtain the ΔTWS estimates associated with our study time window. Complete details of the product can be found in https://grace.jpl.nasa.gov/data/get-data/monthly-mass-grids-land (last access: 15 March 2020).

3.4 Land surface and hydrology models

Soil moisture and TWS can also be derived from land surface or hydrology models at very high spatiotemporal resolution and accuracy, given adequate physics representation and accurate forcing data, and calibrated parameters. Two products are considered in this study, the Global Land Data Assimilation System (GLDAS, Rodell et al. 2004), and the WaterGAP Global Hydrology Model (WGHM; Müller Schmied 2017). The GLDAS-NOAH version 2.1 product provides the near-global water storage components at 0.25° spatial resolution every 3 hours. The soil moisture is modeled in four separate layers (depths), which are 0–10, 10–100, 100–150, and 150–200 cm. Only the top layer soil moisture is used in our analysis based on a consistent soil depth with respect to the satellite soil moisture observation. TWS is constructed by integrating all storage components, i.e., four soil moisture layers, snow water equivalent (SWE), and canopy interception storage. The anthropogenic impact, e.g., irrigation or groundwater pumping, is not included in the GLDAS.

Like the GLDAS, the WGHM also estimates the global water storage (daily at 0.5°×0.5° spatial resolution) but considers both natural hydrological cycles and anthropogenic alterations in the model simulation. Only one soil layer (root zone) is available in the WGHM. TWS is constructed by more comprehensive storage components, including root zone soil moisture, groundwater, SWE, canopy interception, and surface water (e.g., reservoirs, lakes, rivers, or wetlands). The WGHM version 2.2c is used in this study. The model is forced by meteorological forcing data from the WATCH Forcing Data methodology applied to ERA-Interim data and the Climatic Research Unit. A complete WGHM model description can be found in, e.g., Müller Schmied (2017), Müller Schmied et al. (2014).

3.5 Precipitation and streamflow

Precipitation data are obtained from the Tropical Rainfall Measuring Mission (TRMM, Kummerow et al. 1998), a joint mission between NASA and the Japan Aerospace Exploration Agency (JAXA). The daily and monthly precipitation products (TRMM 3B42 and TRMM 3B43 Version 7; Huffman et al. 2007), providing the daily and monthly average precipitation estimates (mm/hr) at a spatial resolution of 0.25° are used in this study. The daily total precipitation (mm/day) is computed by multiplying the data by the number of hours in a day. The monthly total precipitation (mm/month) is computed in the same way, multiplying by the number of hours in a month. Streamflow data are obtained from the Thai Royal Irrigation Department Ministry of Agriculture and Cooperative (http://www.rid.go.th, last accessed: 15 Match 2020). Multiple river gauges are available across the CPB, but most are relatively short or contain significant missing data. Only the C13 station (see Fig. 1a) is used in the analysis because of its long data record with a timespan covering the 2011 flood event.

4 Methods

4.1 Neural network configuration for flood prediction

We evaluate the lead time prediction of flood events using satellite soil moisture observations. The prediction is conducted using a nonlinear autoregressive with an external input network (NARXnet; Menezes and Barreto 2008). The NARXnet is a neural network that learns to predict the temporal pattern using the memory of the time series by itself with the given exogenous information. The network mainly configures with input/output, the hidden layer, and the feedback delays. In this study, the neural network is trained to predict the time series of the flood intensity, e.g., the derived NDWI, given soil moisture retrieval records. The training and prediction phases are conducted using Matlab's deep learning toolbox (Beale et al. 2019), where ten hidden layers with eight-day feedback delays are used. The configuration is found to be optimal after a trial-and-error experiment to balance the computational time and the output accuracy. The network is trained using the Bayesian regularization backpropagation approach, which updates the network's parameters (e.g., weight, bias) by optimizing the contribution of the solution and residual based on the Levenberg-Marquardt optimization (Dan Foresee and Hagan, 1997).

4.2 Close loop evaluation and evaluation metrics

Based on soil moisture-derived NDWI and MODIS-derived NDWI, the closed-loop evaluation (Fig. 2) is performed to assess flood prediction accuracy. At each grid cell, the satellite soil moisture data (m^3/m^3) are used to predict NDWI values of a certain lead time (e.g., eight days), and the result is validated against the MODIS-derived NDWI. For the consistency in the temporal resolution between the input and trained data, only the time period where both the soil moisture and the derived-NDWI are available are used in the evaluation process. The schematic of the evaluation is as follows:

1. The derived-NDWI is spatially resampled (averaging) to the soil moisture grid space to reduce the spatial resolution's inconsistency.

2. At each soil moisture grid cell, the evaluation consists of $N - M \cdot W$ runs; where N is the total number of 8-day time steps in the time series; W is the forecast lead time (e.g., 8-day); and M is the multiplied increment of the time window (e.g., $M = 1$ for 8-day prediction, $M = 2$ for 16-day prediction).
3. For each run (R_i), data of the $N - M \cdot W$ period are used in the training phase, and the remaining $M \cdot W$ data are used in the validation phase. For example, for 8-day prediction (see Fig. 2a), the first run (R_1) uses data from T_1 to T_{N-1} time steps (blue boxes in Fig. 2a) to supervise the neural network, and then the trained network is used to predict the output (NDWI) of the T_N time step (red box in Fig. 2a). Similarly, for the second run (R_2), the training phase uses all data except T_{N-2}, and the prediction is performed at T_{N-1}.
4. In all evaluation runs, a time step prior to the prediction period is used as the initial state, e.g., T_{N-1} for R_1, T_{N-2} for R_2. The process is repeated until R_{N-MW}. The prediction of $T_i < MW$ is omitted due to the unavailability of the initial state.
5. The same concept is applied to predict longer lead times, e.g., 16 or 24 days (see Fig. 2b, 2c). The time series of the predicted output is obtained after all evaluation runs are completed.

At each grid cell, the validation is performed by comparing the prediction (e.g., soil moisture predicted NDWI) with the observation (e.g., MODIS-derived NDWI) in terms of the correlation (ρ) and the root mean squares difference (RMSD) computed as follows:

$$\rho = E[(\boldsymbol{x} - \overline{\boldsymbol{x}})(\boldsymbol{y} - \overline{\boldsymbol{y}})]/\sigma_{\boldsymbol{x}}\sigma_{\boldsymbol{y}} \quad (2)$$

$$RMSD = \sqrt{\frac{\sum(\boldsymbol{x} - \boldsymbol{y})^2}{N - 1}} \quad (3)$$

where $\boldsymbol{x}$ is the vector of the predicted output, $\boldsymbol{y}$ is the observation vector, E[ ] is the expectation operator, and $(\overline{\boldsymbol{x}}, \overline{\boldsymbol{y}})$ and $(\sigma_{\boldsymbol{x}}, \sigma_{\boldsymbol{y}})$ are the mean and standard deviation of $\boldsymbol{x}$ and $\boldsymbol{y}$, respectively.

[Suggested location of Figure 2]

5. Results

5.1 Detecting the extent of the Great Flood of 2011

The MODIS-derived NDWI exhibits the capability to monitor the progression of the Thailand's Great Flood of 2011 (Fig. 3). Monthly derived NDWI over the CPB clearly shows flood features during the 2011 Great Flood (between August 2011 and December 2011) (Fig. 3h – 3l). The inundations begin in the Nan River in August 2011 and progress southward through the Chao Phraya and Tha Chin Rivers in the following months. The maximum inundated areas in the central and southern parts of the CPB are found to be approximately 2,700 km^2 in October 2011 (Fig. 3j) and 3,000 km^2 in November 2011 (Fig. 3k). The central CPB returns to normal (where NDWI values are almost zero) in December 2011. The southern part of the basin exhibits a similar temporal pattern with an approximately one month delay (not shown).

[Suggested location of Figure 3]

Similarly, monthly soil moisture anomalies derived from the SMOS exhibited wetter than usual soils (strong positive anomaly) between August 2011 and December 2011 (Fig. 4h – 4l). The spatial pattern of the abnormally wet soils is consistent with the flood progressive observations from the MODIS-derived NDWI, where the increased moisture is observed over the central CPB in August and then progresses southward toward the southern part in November. However, the spatial pattern of the soil moisture variation is not as localized as the MODIS-derived NDWI due to its resolution being coarser than that of the MODIS product, i.e., ~25 km vs. 500 m, respectively. In addition, the spatial distribution of the soil moisture generally extends beyond the observed surface water. The increased soil moisture does not essentially lead to inundation as long as it is below the soil saturation stage. As such, the spatial distribution of moisture tends to be wider than the flood extent.

[Suggested location of Figure 4]

Meanwhile, the soil moisture anomalies derived from AMSR-E and ASCAT shows a similar monsoon-moisture pattern to that of SMOS (wetter in September – October) (Fig. 5a – 5j). Even though AMSR-E captures the increased soil moisture in the CPB during the flood event (Fig. 5c – 5d), the spatial pattern of the 2011 flood is not as well-defined as SMOS, and the strong surrounding signal makes the flood identification even more difficult. On the other hand, the ASCAT shows very distinct flood features compared to the SMOS and AMSR-E though the flood's spatial pattern is associated with the decreased soil moisture (e.g., Fig. 5g – 5j).

[Suggested location of Figure 5]

Figure 6 demonstrates the daily ASCAT soil moisture retrievals and the associated data flags between 24 October 2011 and 29 October 2011. It is found that the soil moisture over the flood extent is described by either zero, very low (e.g., < 10%), or unresolvable values (Fig. 6a – 6d). The data flags only describe the severe flood locations, while the greater part of the inundated area is unflagged (Fig. 6e – 6h). As such, the saturated soil pixels (near-zero values) remain in our calculation, leading to the flood pattern observed as a negative soil moisture anomaly.

[Suggested location of Figure 6]

The model-derived soil moisture and TWS storage anomalies obtained from the GLDAS and WGHM are shown in Fig. 7. The simulated soil moisture from GLDAS (0-10 cm) and WGHM (root zone) show an agreement with the satellite observations in terms of overall seasonal variation (e.g., wet in September – October, dry in November – December), but no substantial increase in soil moisture is found in response to the 2011 flood (Fig. 7a – 7l). Similarly, modelled-derived TWS shows seasonal variation without the 2011 flood signals (Fig. 7m – 7x). The absence of the flood signature reflects the model limitation to capture soil moisture surplus during flood events. The soil parameter-controlled storage capacity of the model might be inaccurately parameterized or calibrated over the CPB due to the limited availability of in situ data. This could result in overestimated surface runoff, in which water exits the system too quickly and results in little moisture remaining in the soil layer. In contrast to the model simulated TWS, the GRACE-derived ΔTWS depicts the increased TWS during the flood event (Fig. 7y – 7(d1)). However, the spatial distribution and location of the

flood extent are unclear due to the GRACE measurement's limited spatial resolution (~300 km).

[Suggested location of Figure 7]

5.2 Temporal variation associated with the 2011 flood

5.2.1 Assessment of temporal flood detectability

Several flood events occurred over the CPB between 2002 and 2015. Figure 8 shows monthly averaged soil moisture, TWS, precipitation, flood extent, and discharge time series of the central CPB for three flood years (2002, 2006, 2011) compared to their climatology (average over 2002 to 2015). The averaged time series of the southern CPB presents the same temporal pattern (nor shown). Note that the monthly discharge time series is obtained from the measurements at the C13 station (instead of basin average) as it is the only stream gauge measurement available.

[Suggested location of Figure 8]

Most datasets show their most significant variation in 2011, consistent with the most severe flood event and measured discharge during the study period. The MODIS-derived flood extent shows the most consistent trends with the discharge time series, such as a clear flood feature during August and December 2011 (Fig. 8a, 8b). The monthly averaged MODIS-derived NDWI also shows a similar temporal pattern, as in Fig. 8a (not shown). Both MODIS-derived flood extent and measured discharge show similar increased intensity trends in October from 2002, 2006, and 2011. However, the maximum discharges in 2006 and 2011 reach the same value (~3450 m^3/s) even though the flood extent of 2011 is greater by ~23%. This is likely attributed to the limited storage capacity of the stream channel. The discharge in the river channel can only reach the maximum capacity, where the exceeded capacity extends outside the stream channel as a flood. The excessive precipitation over the CPB is attributed to the 2011 flood event (Fig. 8c), where September precipitation is ~26 % greater than the average precipitation observed for the entire year. Similarly, high precipitation observed between August and September 2002 likely induced the 2002 flood. The precipitation in 2006 is greater than the average value in the first half of the year, but no excessive precipitation is detected during the 2006 flood period (e.g., August – October 2006).

SMOS observed the highest soil moisture during the 2011 flood event, approximately 21 % greater than its six-year (2010 – 2015) average values (Fig. 8d). The South Asian monsoon rainfall likely induces the semi-annual cycle, where the first and second peaks in June and October are observed in SMOS-derived soil moisture. The precipitation data from TRMM exhibits a similar semi-annual cycle but a delay of approximately one month (see Fig. 8c). The AMSR-E shows a similar increased soil moisture pattern toward the 2011 flood period (Fig. 8e) even though the complete evaluation of 2011 cannot be performed due to the ended lifetime of the AMSR-E. However, a long record of AMSR-E allows the evaluation of the soil moisture during the 2002 and 2006 flood events, in which the soil moisture shows second and third largest magnitude over the 2002 – 2011 period, respectively. On the other hand, the 2011 soil moisture trend from ASCAT does not correspond to the flood event (Fig. 8f), likely due to the existence of the flagged data in the calculation described in Sect. 5.1.

The GRACE measurement observes a great ΔTWS during the 2002 and 2011 flood periods (Fig. 7g). However, the magnitude of the 2002 ΔTWS is higher than the 2011 ΔTWS value, which contrasts with other observations, e.g., SMOS, AMSR-E, and MODIS. No excessive ΔTWS is detected during the 2006 flood event. A coarse spatial resolution of GRACE (> 300 km) likely explains the inconsistency between GRACE and other datasets. The GRACE derived-ΔTWS is subject to a leakage error (Swenson et al. 2003), in which the surrounding signal likely contaminates the ΔTWS estimate of a small basin (e.g., the CPB). The GLDAS-derived soil moisture fails to capture the flood signatures (Fig. 8h), while the WGHM shows clearer increased moisture associated with the 2006 and 2011 flood events (Fig. 8i). A more comprehensive storage layer (e.g., the inclusion of surface water or groundwater) likely leads to a better performance of the WGHM. However, the WGHM does not show a strong agreement with the MODIS-derived flood extent in both temporal and spatial domains compared to the SMOS and AMSR-E observations.

The Spearman correlation coefficient (ρ) computed between two daily basin-averaged time series with a 0.05 significance level is used to quantify the agreement between different observed variables and the MODIS-derived flood extents (Fig. 9). Only the correlation associated with GRACE data is computed based on the monthly averaged time series due to daily data unavailability. The passive soil moisture retrievals from SMOS and AMSR-E shows significant agreements with the flood extents with the ρ value of about 0.7. The ASCAT shows a negative ρ value among three soil moisture datasets, likely caused by the flagged data elaborated in Sect. 5.1. The precipitation provides a small ρ value (~0.1), which denotes its limitation for flood monitoring (e.g., Sharma et al. 2018). On the contrary, the GRACE and model estimates show reasonable agreements with the flood. The GRACE-derived ΔTWS provides a large ρ value (> 0.5), almost as good as the SMOS or AMSR-E estimate. However, the models provided smaller ρ values of about 0.2 – 0.3, implying the current limitation of using the GLDAS or WGHM to detect flood events. The river gauge measurement shows the most robust connection with the flood extent, with $\rho > 0.8$.

[Suggested location of Figure 9]

5.2.2 Estimation of daily flood lead-time

Two separate daily flood lead-time analyses are conducted for the central and southern CPB. This is mainly to isolate the temporal variation between two neighboring sub-basins, in which their signals associated with the daily flood dynamics might be different. Such analyses can also provide an approximate travel time for the flood to propagate across the basins (e.g., from the central to southern CPB). The daily precipitation (TRMM), soil moisture (SMOS), and discharge during July 2011 and April 2012 are used to assess the lead-time associated with the 2011 flood event. Figure 10 shows the daily basin-average time series of the central CPB and southern CPB. Only soil moisture data from SMOS data are used in the analysis due to the notable flood detection performance and the complete 2011 – 2012 data record elaborated in Sect. 5.1 and Sect. 5.2.1. Because of the C13 station location, the river gauge measurements are assumed to represent the central CPB's integrated response. The daily time series are smoothed using the moving average filter with a 60-day window (selected from the trial and error experiment to determine the optimal fitness while avoiding the over-smoothed result). The phase of the time series (see insert date in Fig. 10) is defined as the calendar date

where the smoothed time series reaches the maximum value, which is found to be between September and November 2011, corresponding to the 2011 flood events.

[Suggested location of Figure 10]

From Fig. 10, the apparent phase shift (time delay) between precipitation, SMOS, and MODIS are observed in both sub-basins. In the central CPB, the precipitation (TRMM) reaches the maximum value on 10 September 2011 (Fig. 10a), approximately two weeks before the peak of soil moisture (SMOS, Fig. 10b). The time delay is attributed to the land surface process mechanism required to redistribute the water through the soil. The flood extent (MOD09) and gauge measurement show the maximum values in the first week of November 2011 (Fig. 10c, 10d), almost two weeks after the soil moisture's peak period. This suggests that soil moisture is likely saturated around the end of October 2011, and additional water throughfall (e.g., incoming water after vegetation interception) can not infiltrate through the soil store but exits the system as surface discharge. The flood extent gradually reduces to almost zero at the end of 2011, where the soil moisture decreases to the average values (~0.3 – 0.4 m^3/m^3). Similar phase shift features are also observed in the southern CPB, but the time delay between the soil moisture and flood extent is found to be slightly shorter. In both sub-basins, SMOS provides valuable information associated with the prediction of flood lead time by about one week or longer.

The phase difference between the central and southern CPB reveals that the precipitation phase (TRMM) remains the same. In contrast, the spatial propagation (from the central to southern CPB) of the soil moisture and flood extent takes over one month. Soil moisture of the southern CPB is higher than the central CPB, likely induced by the multiple sources of water influx into the basin (e.g., precipitation over the basin and floodwater from the central CPB). The different time delays between two sub-basins can also be attributed to geographical factors like the land cover, soil properties, or flood management. However, the detailed investigation of those factors is beyond the scope of this paper. This study fulfills its objective by demonstrating a clear benefit of satellite soil moisture observation (particularly SMOS) as a potential supportive data for flood monitoring.

5.3 The prediction of flood occurrence from SMOS

Significant correlation and lead-time observed between the SMOS soil moisture retrieval and flood extent (Sect. 5.2.2) motivate the SMOS observation to predict the flood occurrence. The evaluation process in Sect. 4 is used to assess the effectiveness of using SMOS to detect the water pixels (e.g., NDWI > 0). At each SMOS grid cell, the daily SMOS observation is trained with the MODIS-derived NDWI via the developed neural network (see network configuration in Sect. 4). Only those days where both SMOS and MODIS data are available are considered in the training or validation phase. The process consists of multiple runs. In each run, the network trained with the available data is used to predict the missing NDWI (see the training-predicting process in Sect. 4). The predicted NDWI (from SMOS) is then validated with the observation (MODIS-derived NDWI) in terms of correlation coefficient and RMSD.

The time series of the SMOS-predicted NDWI between 2010 and 2015 is demonstrated in Fig. 11. The selected grid points (see grid locations, P1, P2, and P3, in Fig. 1) are subject to different land use (see, e.g., http://www.ldd.go.th/ldd_en/en-US/map/map-details/land-use-in-

the-central-region/1; last access: 18 May 2020), e.g., urban (P1), agricultural paddy field (P2), and water body (Pasak Chonlasit Reservoir, P3), which can be used to assess the performance of the trained network with respect to different land surface characteristics. From Fig. 11, the 8-day SMOS-predicted NDWI successfully captures the flood events, observing from a significant agreement with MODIS data (Fig. 11a – 11c). The prediction begins to divert from the observation when the forecast lead time of 16 days or longer is used (see, e.g., Fig. 11d, 11g, 11j). The use of a long forecast lead time leads to a failure to predict the flood occurrence and produces overestimated NDWI values. This suggests that a forecast lead time of 8 days or shorter should be considered over the CPB to maintain the accuracy of the flood predictions. However, in the location with permanent surface water (e.g., point C), the prediction performs equally regardless of the length of lead time. The effective prediction is simply attributed to a similar seasonal pattern of both SMOS and MODIS signals over the inundated area (e.g., high soil moisture results in high surface water). The prediction delivers higher accuracy where both signal characteristics are consistent.

[Suggested location of Figure 11]

The scatter plots (Fig. 12a – 12d) confirm the effectiveness of the SMOS-predicted NDWI, particularly for an 8-day forecast lead time. The difference between the predicted NDWI and the observation diverts from the diagonal with a lead time greater than 16 days (see Fig. 12c, 12d). The diagonal elements observed in, e.g., the 24-day or 32-day prediction, are mainly associated with the grid cells where a substantial seasonal variation of SMOS and MODIS leads to a higher agreement between the predicted and observed NDWI values as seen in Fig. 11c.

[Suggested location of Figure 12]

The CPB-averaged statistical values as a function of the forecast lead time provide an explicit feature of prediction accuracy (Fig. 12e). For example, the estimated correlation and RMSD values are degraded by approximately a factor of four (from ρ = 0.60 to 0.15) and three (from RMSD = 0.09 to 0.30) when the forecast lead time is increased from 8 days to 32 days, respectively. The standard deviation also increases with forecast lead time. Overall, the 8-day prediction shows the most encouraging performance with the correlation value greater than 0.5 and the RMSD value less than 0.1. This aligns with the analysis in Sect. 5.2.2, where the soil moisture observation is found to have a strong temporal correlation with the flood occurrence by approximately one week.

6. Discussion

Satellite data and model simulations demonstrate some capacity for flood detection. Flood inundation inferences derived from the surface reflectance data (e.g., MODIS) provide the most accurate flood intensity/extent estimate in terms of spatial distribution. However, cloud obstruction and limited temporal resolution restrict MODIS data to weekly (i.e., eight days) flood monitoring. In contrast, a sub-daily or higher temporal resolution data is usually required for effective near real-time flood prediction. This study shows that satellite soil moisture information is strongly correlated with flood intensity/occurrence and can be considered supportive data to increase the flood prediction reliability at a sub-weekly timescale. Among the three considered satellite soil moisture observations, the SMOS shows

559 the best agreement with the MODIS-derived flood features in terms of spatial distribution and
560 temporal variation. This is likely attributed to a greater sensible depth (i.e., longer
561 wavelength) of the SMOS sensor, which can observe flood-induced soil saturation more
562 effectively in the CPB than observations associated with shorter wavelengths like those of
563 AMSR-E or ASCAT. This study, for the first time, demonstrates the application of the
564 SMOS-soil moisture flood detection in the CPB, while a similar finding has been previously
565 reported in other regions (e.g., Champagne et al. 2014; Romanov and Khvostov 2015;
566 Ahlmer et al. 2018).

567 AMSR-E observations capture temporal variations associated with flood signals but fail to
568 characterize inundated spatial patterns. The top 2 cm soil layer is likely saturated to a full
569 extent, and C-band observation is unable to distinguish increased soil moisture over the
570 inundated area from conditions in the surrounding environment. Combining AMSR-E data
571 with auxiliary information (e.g., provided by a digital elevation model and a leaf area index),
572 as proposed by Temimi et al. (2010), may offer improvements to flood detection through
573 AMSR-E observations alone. In contrast to limited spatial resolution, AMSR-E observations
574 provide reasonable accuracy in flood timing estimates, reflecting the suitability of using the
575 passive L-band satellite sensor for flood monitoring. In contrast to passive microwave
576 observations, soil moisture retrieval from the active sensor of the ASCAT characterizes the
577 flood as near-zero soil moisture due to the open water detection algorithm that assigned a
578 flagged or small soil moisture value over the inundated areas (e.g., EUMETSAT H-SAF,
579 2017; Brocca et al. 2017). It is noted that although ASCAT observations provide flood-
580 induced soil moisture information in a different form (i.e., as negative values), its spatial
581 feature clearly reflects the flood distribution. In the future, it may be possible to develop an
582 algorithm to transform ASCAT data into the SMOS observation space to exploit the spatial
583 information of ASCAT for flood detection.

584 The relationship between flood and remotely sensed soil moisture data is more reliable than
585 the relationships between flood data and precipitation, model-derived moisture, and GRACE
586 data. The connection between precipitation and flooding is known to be affected by other
587 factors, e.g., land cover (urbanization), catchment characteristics, and climate conditions
588 (e.g., Ahlmer et al. 2018; Sharma et al. 2018), which likely prevent strong linear correlations
589 between the two over the CPB. The weak correlation found in model simulations could be
590 explained by ineffective vertical water redistribution and the absence to account for flooding
591 mechanisms. The model predicts excessive surface runoff and underestimates moisture in the
592 soil store, resulting in faster soil moisture or TWS dry-off than seen through satellite
593 observations (e.g., SMOS, GRACE), as shown in Sect. 5.2.1 (Fig. 8). The GRACE-derived
594 ΔTWS shows a reasonable agreement with the monthly flood timing, in line with previous
595 studies (e.g., Reager et al. 2014; Tangdamrongsub et al. 2016; Gouweleeuw et al. 2018).
596 However, flood feature observations at a sub-monthly resolution or on a fine spatial scale
597 (e.g., < 300 km^2) are hardly possible using GRACE data due to its coarse temporal and
598 spatial resolution.

599 This study also demonstrates that SMOS data can be used to offer flood lead-times of
600 approximately one week or longer, reflecting the potential application of SMOS data in flood
601 forecasting (Giuseppe et al. 2018). The SMOS data also captures progressive flood patterns
602 across sub-basins in both temporal and spatial domains. The neural network constructed to
603 predict flood occurrence (given soil moisture) is found to be sufficiently accurate at certain

forecast lead times. The neural network predictions are more effective with a short lead time (e.g., no more than eight days), likely due to the nonlinearity between soil moisture and flood, as well as the type of data used in the training phase. The difficulty in accurate prediction lies in the fact that wet soil conditions do not necessarily result in flood occurrences. The neural network performs relatively well (i.e., with $\rho \approx 0.6$) over the area where both SMOS and MODIS signals are consistent (e.g., wet soil over water pixels). At the same time, the prediction accuracy is reduced (with an increased forecast lead time) over dry or agricultural areas with occasional flood occurrence. The meaningful representation of data in the trained network also plays a significant role in the prediction accuracy (Najafabadi et al. 2015). In long lead time prediction, the data associated with the flood events are likely absent in the network training, leading to blind predictions of flood occurrences. Higher uncertainty is indeed the result of making predictions with insufficient information (Cortes et al. 1995).

The flood prediction in the CPB is currently limited to the use of digital elevation models and hydrologic simulations (e.g., Pumchawsaun 2018) associated with gauge data to approximate the temporal variation of the flood. However, this approach is difficult in data-sparse regions where gauge data are not available to calibrate the model. The prime advantage of the method introduced in this work is the potentiality of quantifying the flood's lead time approximately in one week by relying only on the freely accessed remotely sensed satellite observational data. This technique allows local flood observatories to obtain needed data for the hydrological model validation that predict runoff and streamflow where none would exist otherwise.

7. Conclusion

This study investigates the potential benefit of using satellite soil moisture retrievals for flood detection, using the Thailand's Great Flood of 2011 as an evaluation scenario. The analyses among three satellite soil moisture observations (AMSR-E, ASCAT, SMOS), different remote sensed datasets (e.g., MODIS, TRMM, GRACE), and model simulations show that SMOS data deliver the best agreement with the flood observations in terms of spatial extent and timing, and also provide an approximate flood lead-time estimate of one week or longer. The performance of the supervised neural network constructed between the SMOS observation and MODIS-derived NDWI depends on the represented (trained) data and land cover. Short-term predictions (e.g., eight days) achieve the best accuracy with an averaged correlation coefficient of 0.6. The application of this approach over the CPB offers clear benefits of SMOS data that could provide some useful assistance for flood monitoring systems. However, the SMOS-informed flood assessment/prediction tool's behavior may vary across regions, and similar evaluations in other study areas will be necessary to confirm the strength of satellite soil moisture data as a tool for flood monitoring. For future work, the use of new satellite soil moisture products, e.g., the enhanced passive soil moisture product of the Soil Moisture Active Passive mission (enhanced-SMAP), Sentinel-1, and the downscale SMOS product, e.g., the Soil Moisture for dEsert Locust early Survey (SMELLS), or the application of a downscaling algorithm could be considered to obtain higher accuracy and higher spatial resolution (e.g., from a few km to down to the several m levels) of soil moisture estimates. This could reduce spatial mismatches between soil moisture retrieval and

satellite imagery data, likely leading to improved flood forecasting performance, particularly at a sub-grid scale (e.g., 500 m – 1 km).

Acknowledgment

NT was supported by the NASA Earth Science Division in support of the National Climate Assessment.

Declarations

Conflicts of interest/Competing interests: Authors declare no conflict of interest

Availability of data and material: Data availability and data access are given in Sect. 3.

References

Adams TE, Pagaon TC (2016) Flood Forecasting: A Global Perspective. Academic Press, Boston, MA, USA. ISBN 9780128018842, doi.org/10.1016/B978-0-12-801884-2.09994-1.

Ahlmer A-K, Cavalli M, Hansson K, et al (2018) Soil moisture remote-sensing applications for identification of flood-prone areas along transport infrastructure. Environ Earth Sci 77:533. https://doi.org/10.1007/s12665-018-7704-z

Ahamed A, Bolten JD (2017) A MODIS-based automated flood monitoring system for southeast asia. Int J. Appl Earth Obs Geoinf 61:104–117. https://doi.org/10.1016/j.jag.2017.05.006

Alvarez-Garreton C, Ryu D, Western AW, et al (2014) The impacts of assimilating satellite soil moisture into a rainfall–runoff model in a semi-arid catchment. J Hydrol 519:2763–2774. https://doi.org/10.1016/j.jhydrol.2014.07.041

Anctil F, Lauzon N, Filion M (2008) Added gains of soil moisture content observations for streamflow predictions using neural networks. J Hydrol 359:225–234. https://doi.org/10.1016/j.jhydrol.2008.07.003

Bajracharya SR, Shrestha MS, Shrestha AB (2017) Assessment of high-resolution satellite rainfall estimation products in a streamflow model for flood prediction in the Bagmati basin, Nepal. J Flood Risk Manag 10:5–16. https://doi.org/10.1111/jfr3.12133

Bauer-Marschallinger B, Freeman V, Cao S, et al (2019) Toward Global Soil Moisture Monitoring With Sentinel-1: Harnessing Assets and Overcoming Obstacles. IEEE Trans Geosci Remote Sens 57:520–539. https://doi.org/10.1109/TGRS.2018.2858004

Beale MH, Hagan MT, Demuth HB (2019) Deep Learning Toolbox: User's Guide for Matlab R2019b, Mathworks

Bidorn B, Chanyotha S, Kish SA, et al (2015) The effects of Thailand′s Great Flood of 2011 on river sediment discharge in the upper Chao Phraya River basin, Thailand. Int J Sediment Res 30:328–337. https://doi.org/10.1016/j.ijsrc.2015.10.001

Bitar AA, Mialon A, Kerr YH, et al (2017) The global SMOS Level 3 daily soil moisture and brightness temperature maps. Earth Syst Sci Data 9:293–315. https://doi.org/10.5194/essd-9-293-2017

Brocca L, Crow WT, Ciabatta L, et al (2017) A Review of the Applications of ASCAT Soil Moisture Products. IEEE J Sel Top Appl Earth Obs Remote Sens 10:2285–2306. https://doi.org/10.1109/JSTARS.2017.2651140

Brodzik MJ, Billingsley B, Haran T, et al (2012) EASE-Grid 2.0: Incremental but Significant Improvements for Earth-Gridded Data Sets. ISPRS Int J Geo-Inf 1:32–45. https://doi.org/10.3390/ijgi1010032

Chan SK, Bindlish R, O'Neill P, et al (2018) Development and assessment of the SMAP enhanced passive soil moisture product. Remote Sens Environ 204:931–941. https://doi.org/10.1016/j.rse.2017.08.025

Champagne C, Davidson A, Cherneski P, et al (2014) Monitoring Agricultural Risk in Canada Using L-Band Passive Microwave Soil Moisture from SMOS. J Hydrometeor 16:5–18. https://doi.org/10.1175/JHM-D-14-0039.1

Cortes C, Jackel LD, Chiang W-P (1995) Limits on Learning Machine Accuracy Imposed by Data Quality. In: Tesauro G, Touretzky DS, Leen TK (eds) Adv Neural Inform Process Syst 7. MIT Press, pp 239–246

Coumou D, Rahmstorf S (2012) A decade of weather extremes. Nat Clim Change 2:491–496. https://doi.org/10.1038/nclimate1452

Cruz FRG, Binag MG, Ga MRG, Uy FAA (2018) Flood Prediction Using Multi-Layer Artificial Neural Network in Monitoring System with Rain Gauge, Water Level, Soil Moisture Sensors. In: TENCON 2018 - 2018 IEEE Region 10 Conference. pp 2499–2503

Dan Foresee F, Hagan MT (1997) Gauss-Newton approximation to Bayesian learning. In: Proceedings of International Conference on Neural Networks (ICNN'97). pp 1930–1935 vol.3

Eltahir EAB (1998) A Soil Moisture–Rainfall Feedback Mechanism: 1. Theory and observations. Water Resour Res 34:765–776. https://doi.org/10.1029/97WR03499

Entekhabi D, Njoku EG, O'Neill PE, et al (2010) The Soil Moisture Active Passive (SMAP) Mission. Proc IEEE 98:704–716. https://doi.org/10.1109/JPROC.2010.2043918

Escorihuela MJ, Merlin O, Stefan V, et al (2018) SMOS based high resolution soil moisture estimates for desert locust preventive management. Remote Sens Appl Soc Environ 11:140–150. https://doi.org/10.1016/j.rsase.2018.06.002

EUMETSAT H-SAF (2017) Algorithm Theoretical Baseline Document (ATBD) Metop ASCAT Soil Moisture CDR and offline products. Available online: http://hsaf.meteoam.it/documents/ATDD/ASCAT_SSM_CDR_ATBD_v0.5.pdf (last access: 20 May 2020)

Farahani HH, Ditmar P, Inácio P, et al (2017) A high resolution model of linear trend in mass variations from DMT-2: Added value of accounting for coloured noise in GRACE data. J. Geodyn 103:12–25. https://doi.org/10.1016/j.jog.2016.10.005

Few R (2003) Flooding, vulnerability and coping strategies: local responses to a global threat. Prog Dev Stud 3:43–58. https://doi.org/10.1191/1464993403ps049ra

Han J, Tangdamrongsub N, Hwang C, Abidin HZ (2017) Intensified water storage loss by biomass burning in Kalimantan: Detection by GRACE. J Geophys Res Solid Earth 122:2017JB014129. https://doi.org/10.1002/2017JB014129

Hirabayashi Y, Mahendran R, Koirala S, et al (2013) Global flood risk under climate change. Nat Clim Change 3:816–821. https://doi.org/10.1038/nclimate1911

Giuseppe FD, Baugh C, Prudhomme C, Thiemert D (2018) Can SMOS data support flood and fire forecasts? The ECMWF Newsletter 157. Available online: https://www.ecmwf.int/en/newsletter/157/news/can-smos-data-support-flood-and-fire-forecasts (last access: 22 March 2020)

737 Gouweleeuw BT, Kvas A, Gruber C, et al (2018) Daily GRACE gravity field solutions track
738 major flood events in the Ganges–Brahmaputra Delta. Hydrol Earth Syst Sci
739 22:2867–2880. https://doi.org/10.5194/hess-22-2867-2018
740 Hossain F, Anagnostou EN (2004) Assessment of current passive-microwave- and infrared-
741 based satellite rainfall remote sensing for flood prediction. J Geophys Res
742 Atmospheres 109. https://doi.org/10.1029/2003JD003986
743 Huffman GJ, Bolvin DT, Nelkin EJ, et al (2007) The TRMM Multisatellite Precipitation
744 Analysis (TMPA): Quasi-Global, Multiyear, Combined-Sensor Precipitation
745 Estimates at Fine Scales. J Hydrometeor 8:38–55. https://doi.org/10.1175/JHM560.1
746 Jamrussri S, Toda Y (2017) Simulating past severe flood events to evaluate the effectiveness
747 of nonstructural flood countermeasures in the upper Chao Phraya River Basin,
748 Thailand. J Hydrol Reg Stud 10:82–94. https://doi.org/10.1016/j.ejrh.2017.02.001
749 Karthikeyan L, Pan M, Wanders N, et al (2017) Four decades of microwave satellite soil
750 moisture observations: Part 1. A review of retrieval algorithms. Adv Water Resour
751 109:106–120. https://doi.org/10.1016/j.advwatres.2017.09.006
752 Khan SI, Hong Y, Wang J, et al (2011) Satellite Remote Sensing and Hydrologic Modeling
753 for Flood Inundation Mapping in Lake Victoria Basin: Implications for Hydrologic
754 Prediction in Ungauged Basins. IEEE Trans Geosci Remote Sens 49:85–95.
755 https://doi.org/10.1109/TGRS.2010.2057513
756 Komi K, Neal J, Trigg MA, Diekkrüger B (2017) Modelling of flood hazard extent in data
757 sparse areas: a case study of the Oti River basin, West Africa. J Hydrol Reg Stud
758 10:122–132. https://doi.org/10.1016/j.ejrh.2017.03.001
759 Koster RD, Dirmeyer PA, Guo Z, et al (2004) Regions of Strong Coupling Between Soil
760 Moisture and Precipitation. Science 305:1138–1140.
761 https://doi.org/10.1126/science.1100217
762 Koster RD, Suarez MJ (2001) Soil Moisture Memory in Climate Models. J Hydrometeor
763 2:558–570. https://doi.org/10.1175/1525-7541(2001)002<0558:SMMICM>2.0.CO;2
764 Kummerow C, Barnes W, Kozu T, et al (1998) The Tropical Rainfall Measuring Mission
765 (TRMM) Sensor Package. J Atmos Oceanic Technol 15:809–817.
766 https://doi.org/10.1175/1520-0426(1998)015<0809:TTRMMT>2.0.CO;2
767 Kure S, Tebakari T (2012) Hydrological impact of regional climate change in the Chao
768 Phraya River Basin, Thailand. Hydrol Res Lett 6:53–58.
769 https://doi.org/10.3178/hrl.6.53
770 Kwak Y, Park J, Yorozuya A, Fukami K (2012) Estimation of flood volume in Chao Phraya
771 River basin, Thailand, from MODIS images couppled with flood inundation level. In:
772 2012 IEEE IGARSS, pp 887–890
773 Lebel L, Manuta JB, Garden P (2011) Institutional traps and vulnerability to changes in
774 climate and flood regimes in Thailand. Reg Environ Change 11:45–58.
775 https://doi.org/10.1007/s10113-010-0118-4
776 Lin Moe T, Pathranarakul P (2006) An integrated approach to natural disaster management:
777 Public project management and its critical success factors. Disaster Prev Manag
778 15:396–413. https://doi.org/10.1108/09653560610669882
779 Long D, Shen Y, Sun A, et al (2014) Drought and flood monitoring for a large karst plateau
780 in Southwest China using extended GRACE data. Remote Sens Environ 155:145–
781 160. https://doi.org/10.1016/j.rse.2014.08.006
782 Longuevergne L, Wilson CR, Scanlon BR, Crétaux JF (2013) GRACE water storage
783 estimates for the Middle East and other regions with significant reservoir and lake
784 storage. Hydrol Earth Syst Sci 17:4817–4830. https://doi.org/10.5194/hess-17-4817-
785 2013

786 Maggioni V, Sapiano MRP, Adler RF (2016) Estimating Uncertainties in High-Resolution
787 Satellite Precipitation Products: Systematic or Random Error? J Hydrometeor
788 17:1119–1129. https://doi.org/10.1175/JHM-D-15-0094.1
789 Massari C, Brocca L, Moramarco T, et al (2014) Potential of soil moisture observations in
790 flood modelling: Estimating initial conditions and correcting rainfall. Adv Water
791 Resour 74:44–53. https://doi.org/10.1016/j.advwatres.2014.08.004
792 Mei Y, Anagnostou EN, Nikolopoulos EI, Borga M (2014) Error Analysis of Satellite
793 Precipitation Products in Mountainous Basins. J Hydrometeor 15:1778–1793.
794 https://doi.org/10.1175/JHM-D-13-0194.1
795 Menezes JMP, Barreto GA (2008) Long-term time series prediction with the NARX network:
796 An empirical evaluation. Neurocomputing 71:3335–3343.
797 https://doi.org/10.1016/j.neucom.2008.01.030
798 Mirza MMQ (2003) Climate change and extreme weather events: can developing countries
799 adapt? Clim. Policy 3:233–248. https://doi.org/10.3763/cpol.2003.0330
800 Mikhailov VN, Nikitina OI (2009) Hydrological and morphological processes in the Chao
801 Phraya Mouth Area (Thailand) and their anthropogenic changes. Water Resour
802 36:613. https://doi.org/10.1134/S0097807809060013
803 Müller Schmied H (2017) Evaluation, modification and application of a global hydrological
804 model. Doctoral Thesis. Institute of Physical Geography, Goethe University
805 Frankfurt, Frankfurt am Main. urn:nbn:de:hebis:30:3-440735
806 Müller Schmied H, Eisner S, Franz D, et al (2014) Sensitivity of simulated global-scale
807 freshwater fluxes and storages to input data, hydrological model structure, human
808 water use and calibration. Hydrol Earth Syst Sci 18:3511–3538.
809 https://doi.org/10.5194/hess-18-3511-2014
810 Najafabadi MM, Villanustre F, Khoshgoftaar TM, et al (2015) Deep learning applications
811 and challenges in big data analytics. J Big Data 2:1. https://doi.org/10.1186/s40537-
812 014-0007-7
813 Njoku EG, Jackson TJ, Lakshmi V, et al (2003) Soil moisture retrieval from AMSR-E. IEEE
814 Trans Geosci Remote Sens 41:215–229. https://doi.org/10.1109/TGRS.2002.808243
815 Pitman AJ (2003) The evolution of, and revolution in, land surface schemes designed for
816 climate models. Int J Climatol 23:479–510. https://doi.org/10.1002/joc.893
817 Pumchawsaun P (2018) Integrated hydrodynamic and socio-economic damage modelling for
818 assessment of flood risk in large-scale basin: The case study of Lower Chao Phraya
819 River Basin in Thailand. Master thesis. Stockholm University, Faculty of Science,
820 Department of Physical Geography. p.64. urn:nbn:se:su:diva-157381
821 Rakwatin P, Sansena T, Marjang N, Rungsipanich A (2013) Using multi-temporal remote-
822 sensing data to estimate 2011 flood area and volume over Chao Phraya River basin,
823 Thailand. Remote Sens Lett 4:243–250.
824 https://doi.org/10.1080/2150704X.2012.723833
825 Ray RL, Jacobs JM (2007) Relationships among remotely sensed soil moisture, precipitation
826 and landslide events. Nat Hazards 43:211–222. https://doi.org/10.1007/s11069-006-
827 9095-9
828 Reager JT, Thomas BF, Famiglietti JS (2014) River basin flood potential inferred using
829 GRACE gravity observations at several months lead time. Nat Geosci 7:588–592.
830 https://doi.org/10.1038/ngeo2203
831 Rodell M, Houser PR, Jambor U, et al (2004) The Global Land Data Assimilation System.
832 Bull Amer Meteor Soc 85:381–394. https://doi.org/10.1175/BAMS-85-3-381
833 Romanov AN, Khvostov IV (2015) Microwave Remote Monitoring of Altai Catastrophic
834 Flood Dynamics Using SMOS Data. IEEE Geosci Remote Lett 12:2036–2040.
835 https://doi.org/10.1109/LGRS.2015.2444592

836 Sanyal J, Carbonneau P, Densmore AL (2013) Hydraulic routing of extreme floods in a large
837 ungauged river and the estimation of associated uncertainties: a case study of the
838 Damodar River, India. Nat Hazards 66:1153–1177. https://doi.org/10.1007/s11069-
839 012-0540-7
840 Senanayake IP, Yeo I-Y, Tangdamrongsub N, et al (2019) An in-situ data based model to
841 downscale radiometric satellite soil moisture products in the Upper Hunter Region of
842 NSW, Australia. J Hydrol 572:820–838. https://doi.org/10.1016/j.jhydrol.2019.03.014
843 Sharma A, Wasko C, Lettenmaier DP (2018) If Precipitation Extremes Are Increasing, Why
844 Aren't Floods? Water Resour Res 54:8545–8551.
845 https://doi.org/10.1029/2018WR023749
846 Shook G (1997) An assessment of Disaster Risk and its Management in Thailand. Disasters
847 21:77–88. https://doi.org/10.1111/1467-7717.00045
848 Smith LC (1997) Satellite remote sensing of river inundation area, stage, and discharge: a
849 review. Hydrol Process 11:1427–1439. https://doi.org/10.1002/(SICI)1099-
850 1085(199708)11:10<1427::AID-HYP473>3.0.CO;2-S
851 Swenson S, Wahr J, Milly PCD (2003) Estimated accuracies of regional water storage
852 variations inferred from the Gravity Recovery and Climate Experiment (GRACE).
853 Water Resour Res 39:. https://doi.org/10.1029/2002WR001808
854 Tangdamrongsub N, Ditmar PG, Steele-Dunne SC, et al (2016) Assessing total water storage
855 and identifying flood events over Tonlé Sap basin in Cambodia using GRACE and
856 MODIS satellite observations combined with hydrological models. Remote Sens
857 Environ 181:162–173. https://doi.org/10.1016/j.rse.2016.03.030
858 Tapley BD, Bettadpur S, Ries JC, et al (2004) GRACE Measurements of Mass Variability in
859 the Earth System. Science 305:503–505. https://doi.org/10.1126/science.1099192
860 Temimi M, Leconte R, Chaouch N, et al (2010) A combination of remote sensing data and
861 topographic attributes for the spatial and temporal monitoring of soil wetness. J
862 Hydrol 388:28–40. https://doi.org/10.1016/j.jhydrol.2010.04.021
863 Toth E, Brath A, Montanari A (2000) Comparison of short-term rainfall prediction models
864 for real-time flood forecasting. J Hydrol 239:132–147. https://doi.org/10.1016/S0022-
865 1694(00)00344-9
866 Tramblay Y, Bouvier C, Martin C, et al (2010) Assessment of initial soil moisture conditions
867 for event-based rainfall–runoff modelling. J Hydrol 387:176–187.
868 https://doi.org/10.1016/j.jhydrol.2010.04.006
869 Vermote EF, Roger JC, Ray JP (2015). MODIS surface reflectance user's guide version 1.4.
870 Technical report. http://modis-sr.ltdri.org/guide/MOD09_UserGuide_v1.4.pdf, last
871 access: 32 May 2020
872 Wanders N, Karssenberg D, Roo A de, et al (2014) The suitability of remotely sensed soil
873 moisture for improving operational flood forecasting. Hydrol Earth Syst Sci 18:2343–
874 2357. https://doi.org/10.5194/hess-18-2343-2014
875 Wagner W, Lemoine G, Rott H (1999) A Method for Estimating Soil Moisture from ERS
876 Scatterometer and Soil Data. Remote Sens Environ 70:191–207.
877 https://doi.org/10.1016/S0034-4257(99)00036-X
878 World Bank (2012) Thai flood 2011: Rapid assessment for resilient recovery and
879 reconstruction planning. Available online:
880 https://openknowledge.worldbank.org/handle/10986/26862, last access: 21 May 2020
881 Wu H, Adler RF, Tian Y, et al (2014) Real-time global flood estimation using satellite-based
882 precipitation and a coupled land surface and routing model. Water Resour Res
883 50:2693–2717. https://doi.org/10.1002/2013WR014710

884 Zhou H, Luo Z, Tangdamrongsub N, et al (2018) Identifying Flood Events over the Poyang
885 Lake Basin Using Multiple Satellite Remote Sensing Observations, Hydrological
886 Models and In Situ Data. Remote Sens 10:713. https://doi.org/10.3390/rs10050713

887 Table 1: Characteristics of satellite soil moisture data used in this study.

	SMOS	**AMSR-E**	**ASCAT**
Frequency	1.4 GHz (L-band)	6.9 GHz (C-band)	5.255 GHz (C-band)
Sampling grid size	~25 km	25 km	12.5 km
Approximate depth	~5 cm	~2 cm	~2 cm
Data availability	2010 – Present	2002 – 2011	2007 – Present
Data access (last access: 15 March 2020)	https://www.catds.fr	https://disc.gsfc.nasa.gov	http://hsaf.meteoam.it/soil-moisture.php

888

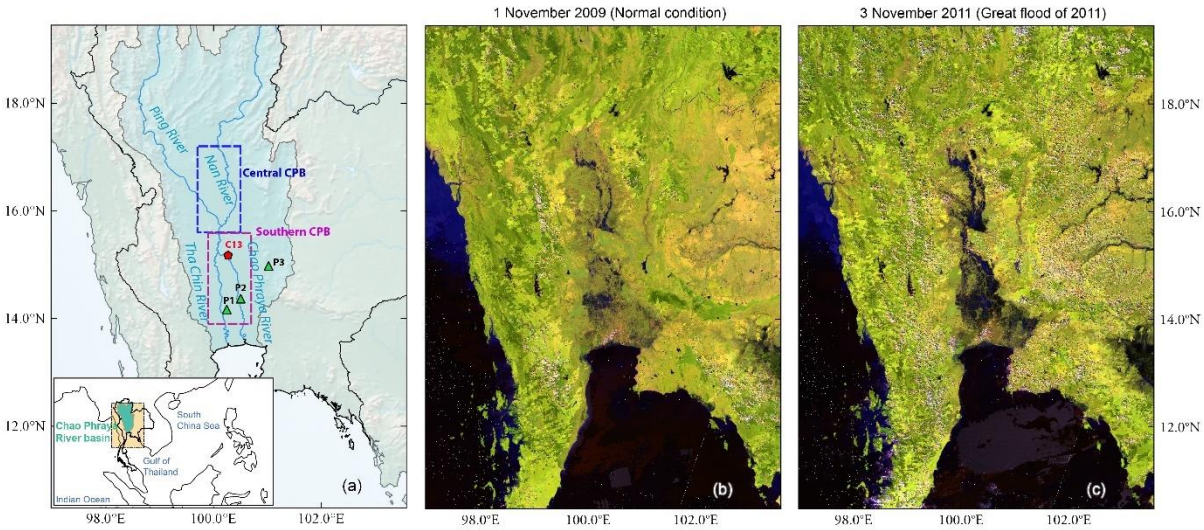

Fig. 1 (a) The Chao Phraya River Basin (CPB) in central Thailand. The blue and magenta boundaries indicate the central and southern CPB, while the points P1 – P3 are the locations associated with different land use discussed in the Results section. The location of stream gauge C13 is also shown. (b - c) The natural images of MODIS reflectance data on 1 November 2009 (normal condition) and 3 November 2011 (during the Thailand's Great Flood of 2011).

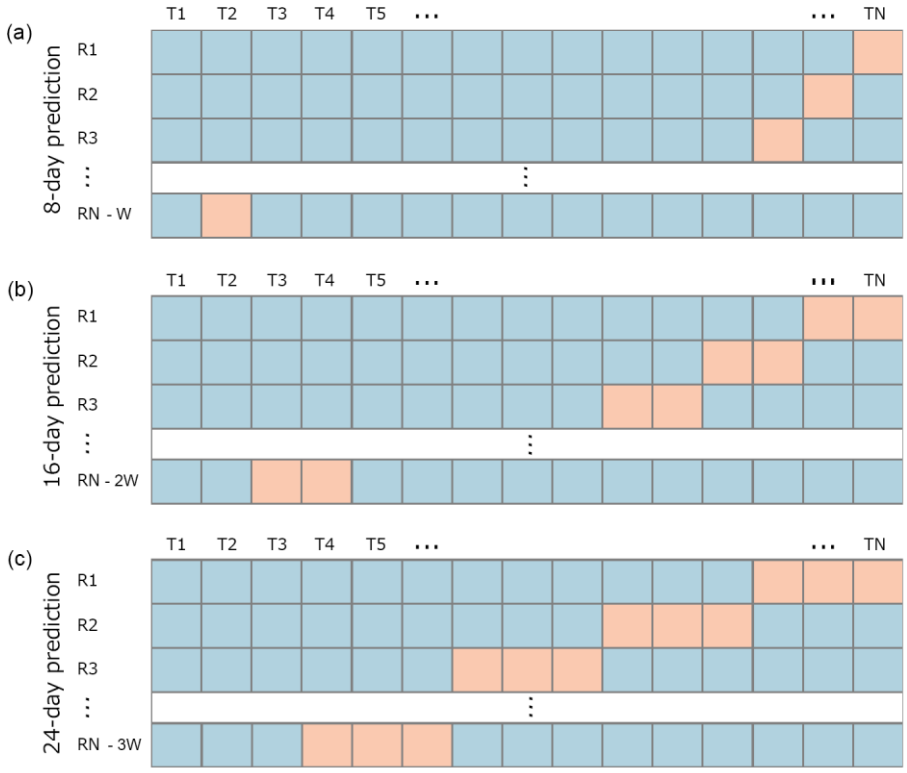

Fig. 2 Evaluation scheme for flood prediction associated with different forecast lead time (a) 8 days, (b) 16 days, and (c) 24 days. A box (square) represents an 8-day time interval. The blue shade represents the data used in the training phase, while the orange indicates the validated phase. The comprehensive evaluation process is described in Sect. 4.

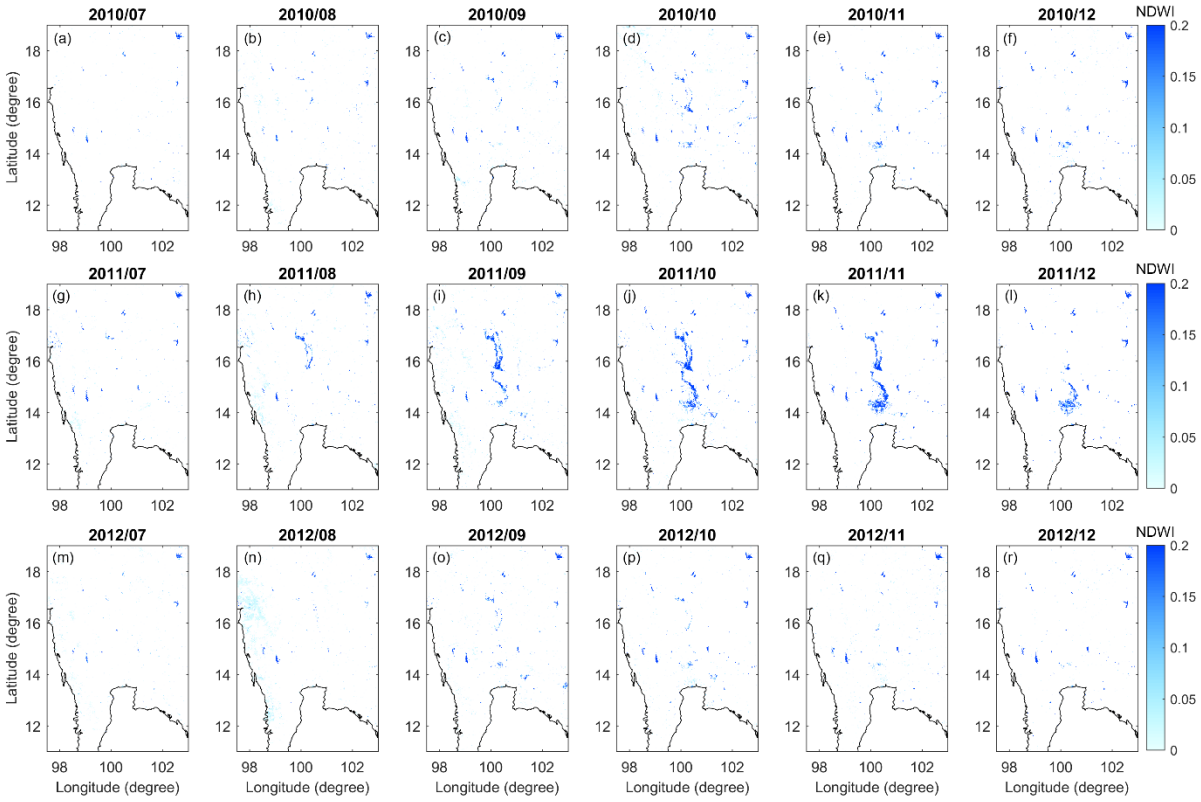

Fig. 3 The monthly-averaged MODIS-derived NDWI over the CPB in the second half (July – December) of 2010 (first row), 2011 (middle row), and 2012 (bottom row), respectively.

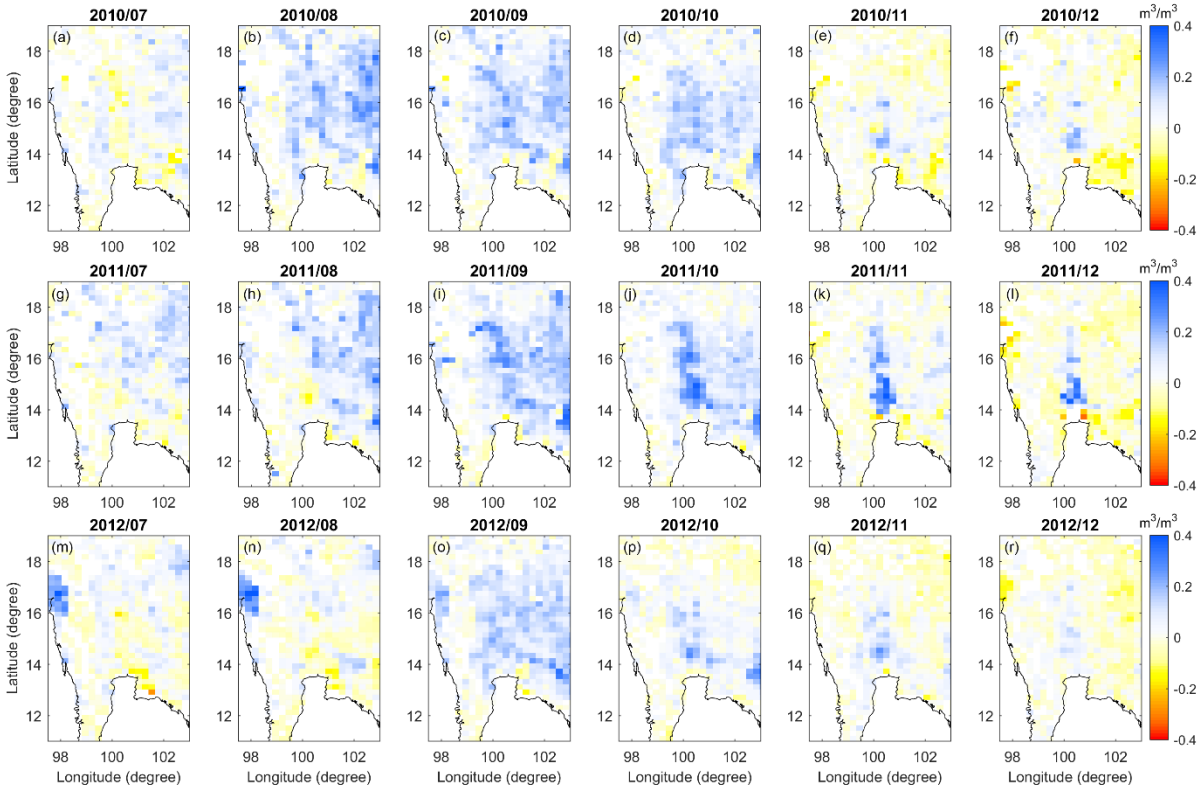

Fig. 4 The monthly-averaged soil moisture anomalies derived from the daily SMOS data over the CPB in the second half (July – December) of 2010 (first row), 2011 (middle row), and 2012 (bottom row), respectively. The anomaly is computed by removing the long-term mean soil moisture estimate from the daily data.

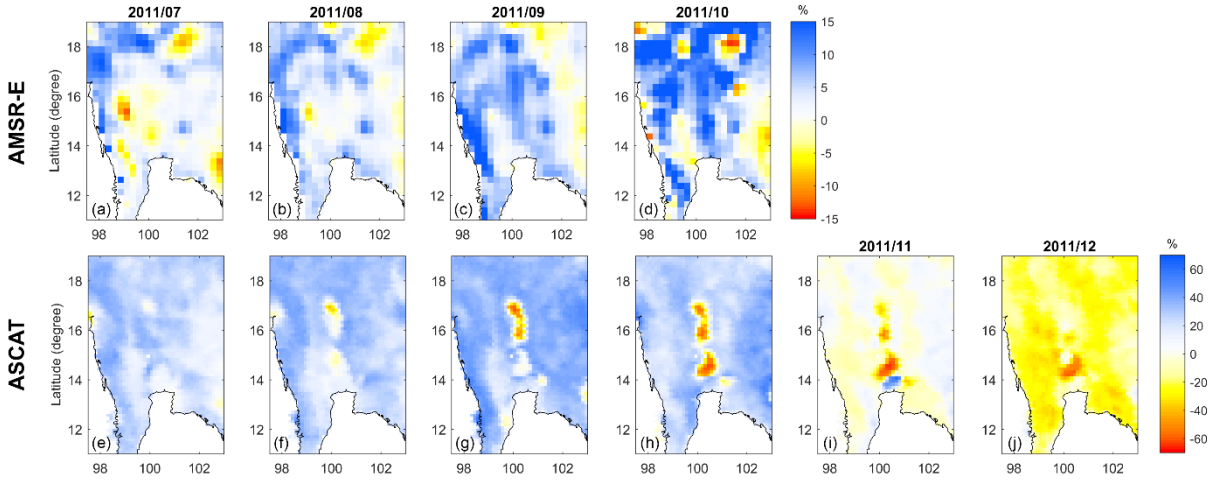

909

910 **Fig. 5** Similar to Fig. 4, but for AMSE-R (top row) and ASCAT (bottom row) during the
911 Thailand's Great Flood of 2011 (July – December 2011).

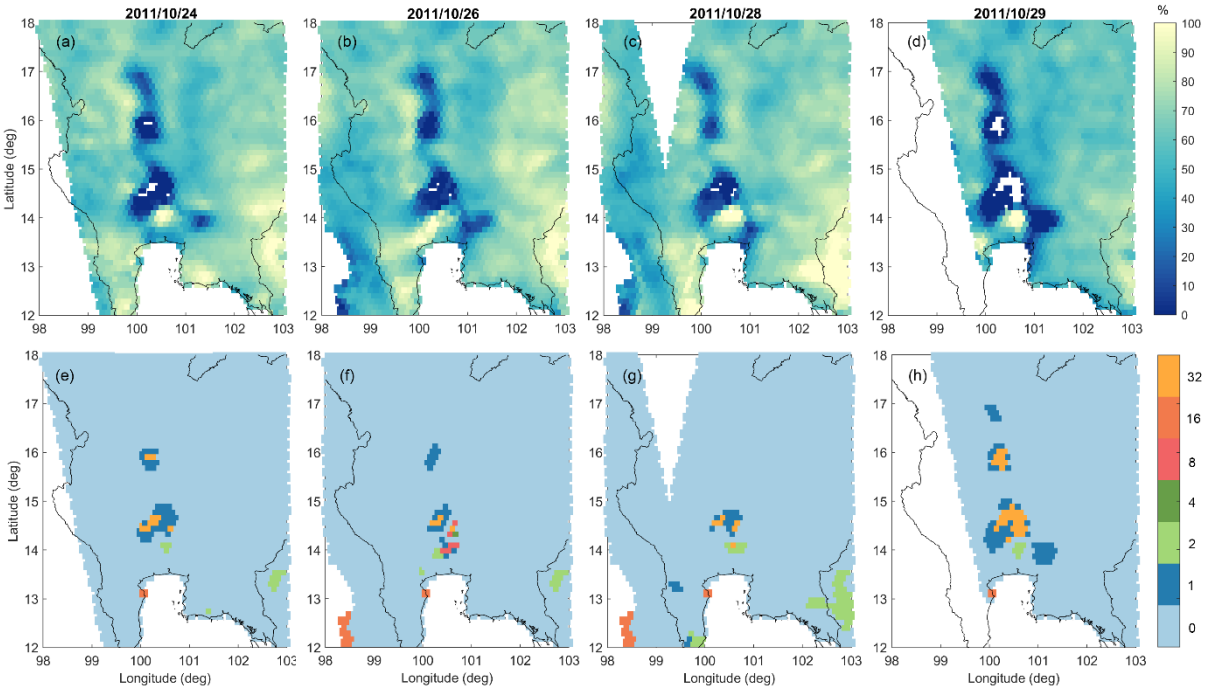

912

913 **Fig. 6** The daily degree of saturation (top) and the associated data flag (bottom) obtained
914 from the ASCAT data between 24 October 2011 and 29 October 2011. Only days with
915 available soil moisture measurements over the CPB are shown. The pixel with Not a Number
916 (NaN) value is shown as white. Based on the ASCAT data description (EUMETSAT H-SAF,
917 2007), a certain value of soil moisture (SM) value is given when the flag is presented, e.g., 0:
918 Normal SM value, 1: SM is set to 0 % (-25 % < SM < 0 %), 2: SM is set to 100 % (100 % <
919 SM < 125 %), 4: SM is set to NaN (SM < -25 %), 8: SM is set to NaN (SM > 125 %), 16:
920 Normal SM value (after wet correction applied), 32: SM is set to NaN (backscatter is not
921 usable). A comprehensive description of the ASCAT data can be found in EUMETSAT H-
922 SAF (2007).

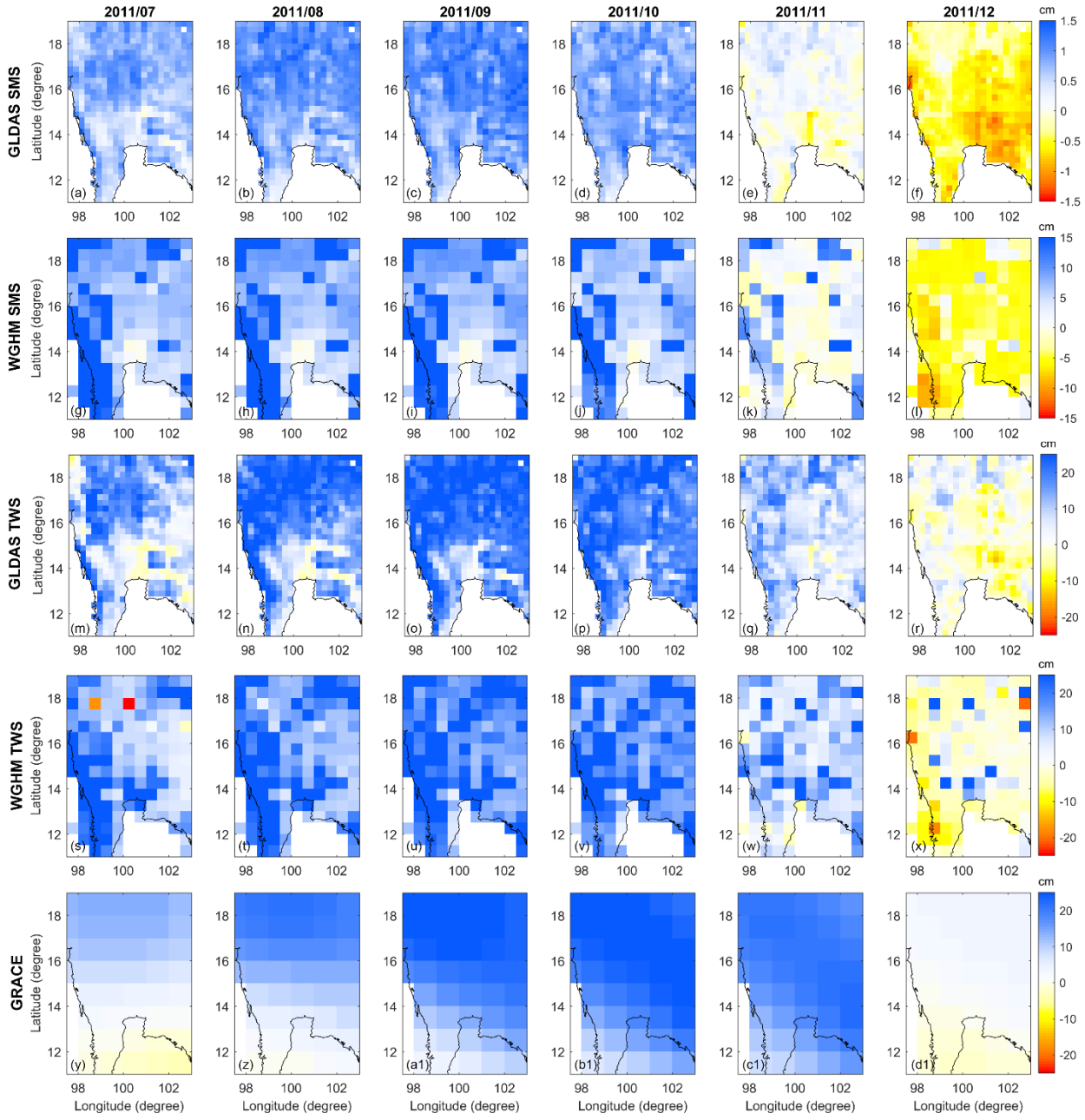

Fig. 7 The soil moisture storage (SMS) and TWS anomalies obtained from model simulations and GRACE data during the 2011 Thailand's Great Flood period (July – December 2011).

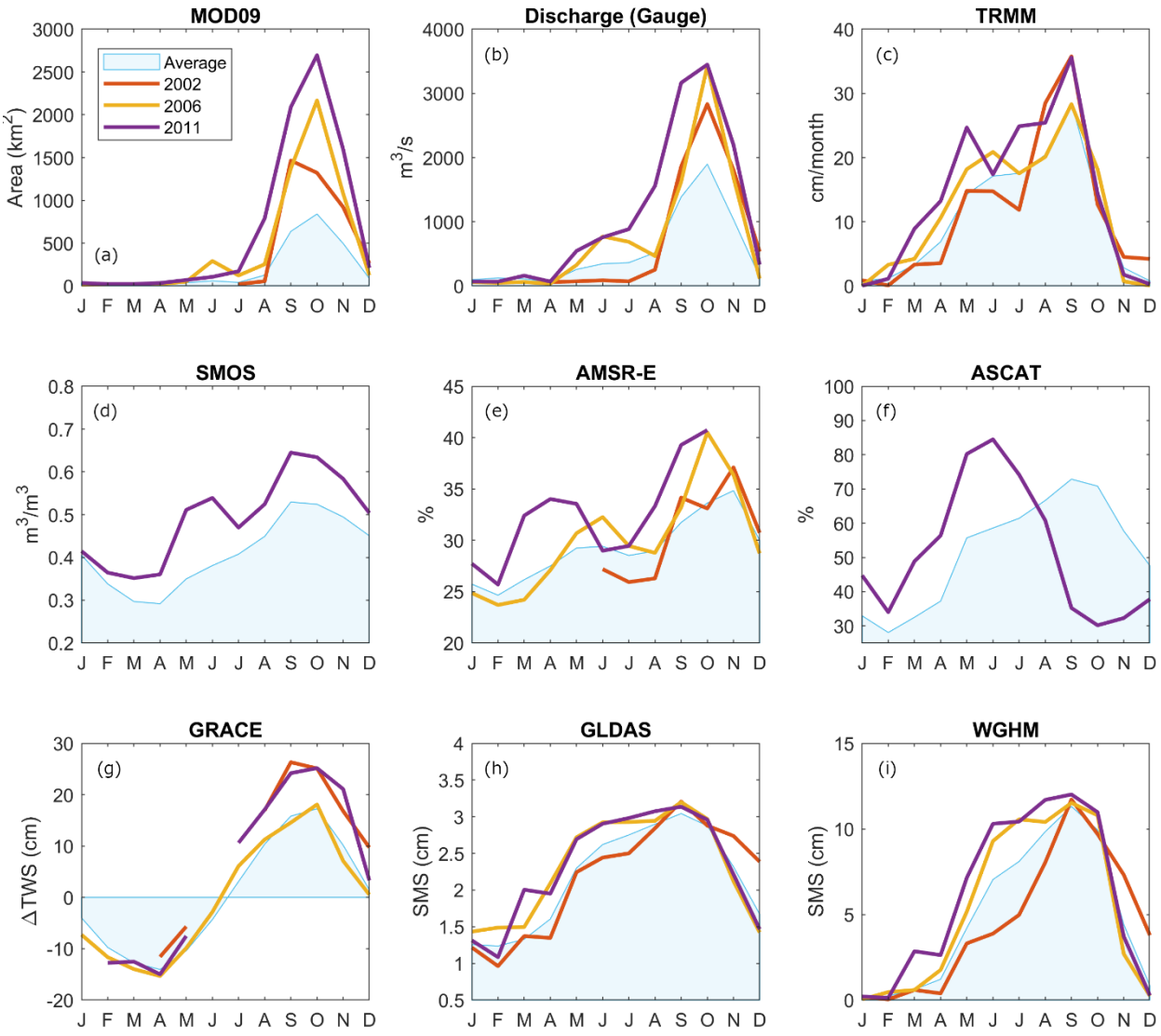

Fig. 8 The monthly time series averaged over the central CPB obtained different observations, (a) MODIS-derived flood extent, (b) C13 Gauge measurement, (c) TRMM-derived precipitation, (d) SMOS, (e) AMSR-E, (f) ASCAT, (g) GRACE, (h) GLDAS-derived soil moisture storage (SMS), and (i) WGHM-derived SMS. The time series associated with severe flood years (2002, 2006, and 2011) are shown as separate solid lines. The monthly climatology (average) computed between 2002 and 2015 is also shown as a shaded area.

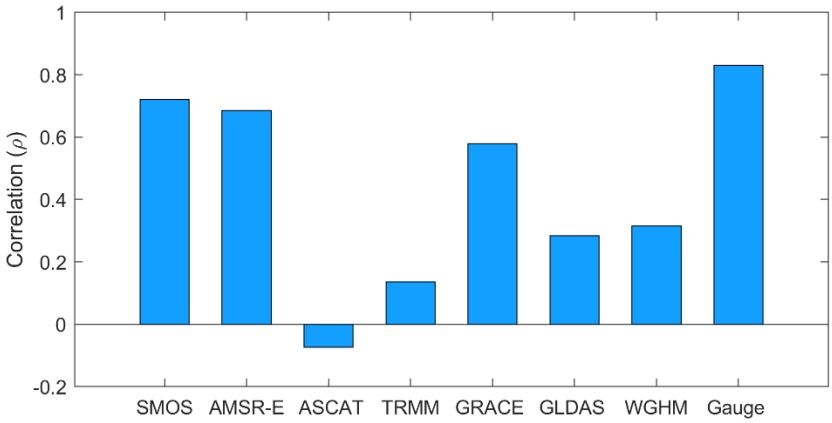

Fig. 9 The correlation coefficient computed from different datasets with respect to the MODIS-derived flood extent in the central CPB. The value of the southern CPB shows a similar result (not shown).

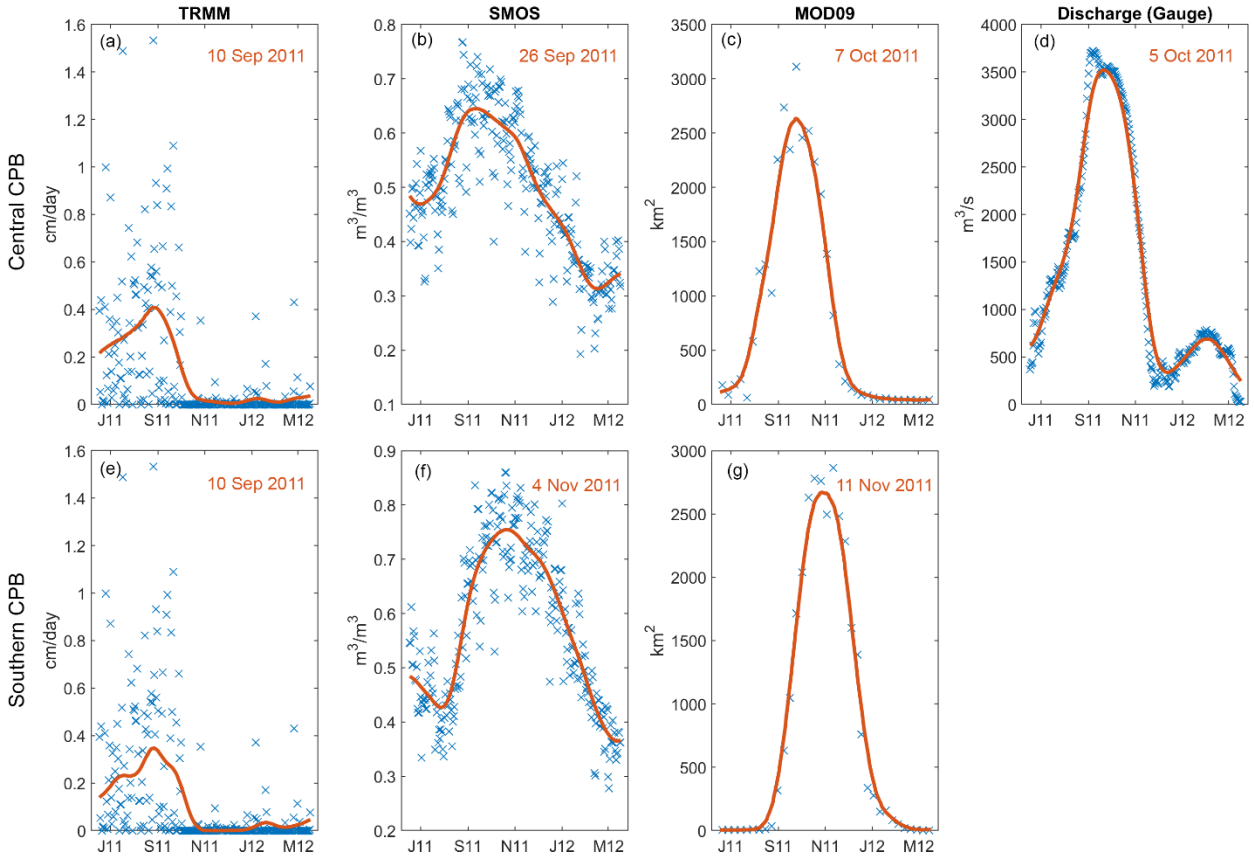

Fig. 10 The daily time series of the TRMM-derived precipitation (first column), SMOS-derived soil moisture (second column), MODIS-derived flood extent (third column), and stream gauge measurements (first column) in the central (first row) and southern CPB (second row) between July 2011 and March 2012. The daily measurement is shown in a cross (x), while the smoothed time series is shown as a solid line. The calendar date when the smooth time series reach the peak is given in each subplot. The horizontal tick label represents day 15 of the month.

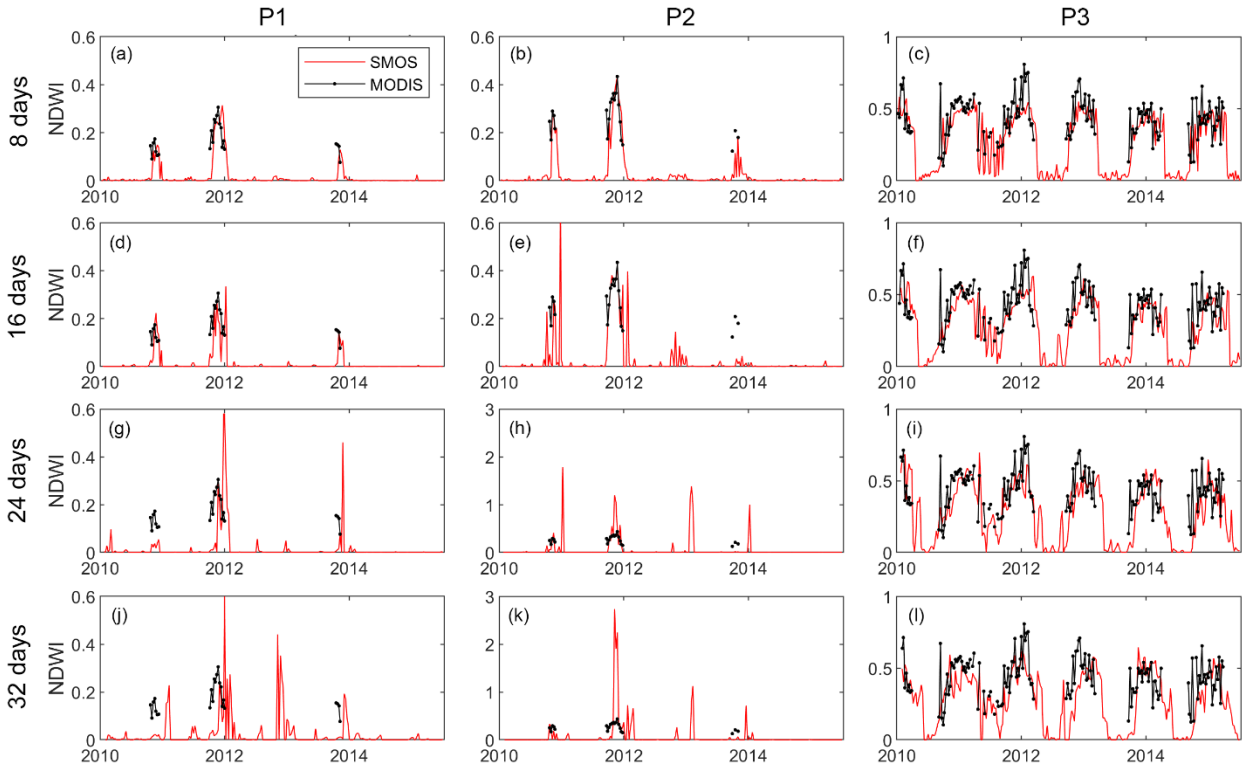

945

946 **Fig. 11** The SMOS-predicted NDWI time series from the neural network as a function of
947 forecast lead time (e.g., 8 days (first row), 16 days (second row), 24 days (third row), and 32
948 days (fourth row)) in three different locations associated with different land cover, (P1)
949 urban, (P2) agricultural field, and (P3) water body (see locations in Fig. 1). The MODIS-
950 derived NDWI is also shown.

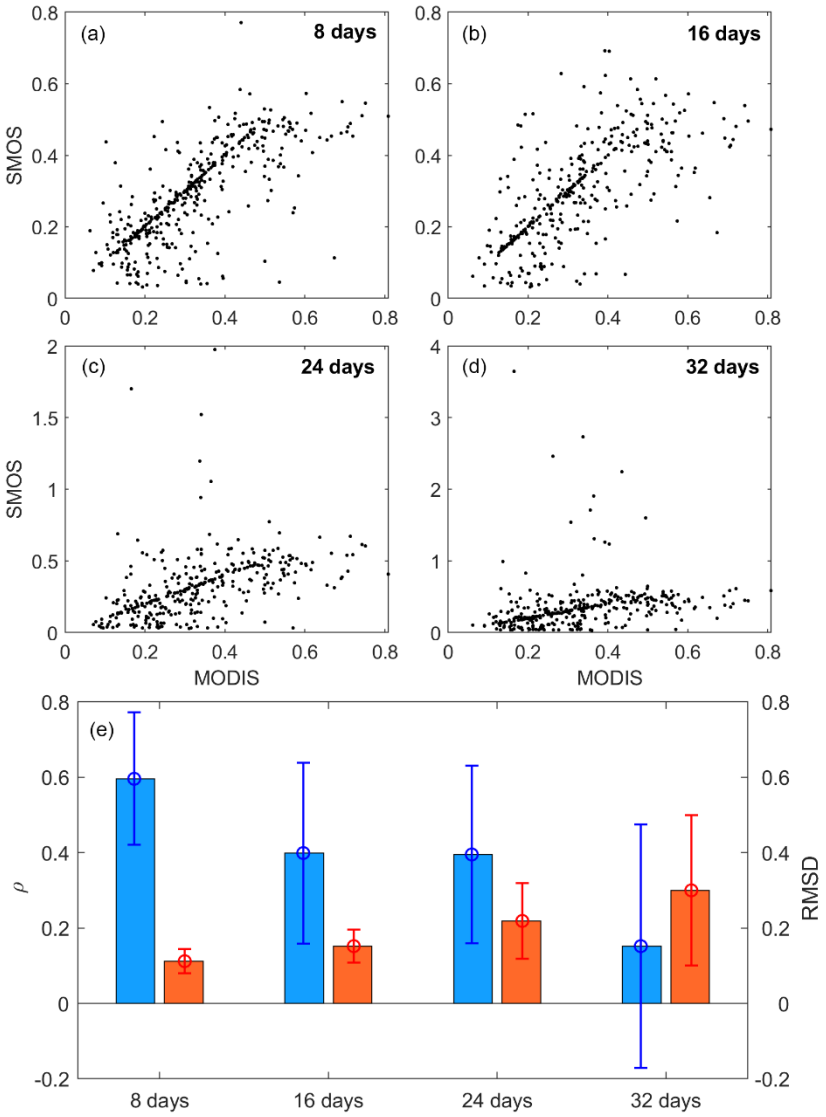

Fig. 12 Scatter plots of NDWI values between the SMOS prediction and MODIS as a function of predicted time windows, (a) 8 days, (b) 16 days, (c) 24 days, and (d) 32 days. (e) The basin averaged statistical values (correlation coefficient (ρ, blue) and RMSD (red)) computed between the SMOS-predicted and MODIS-derived NDWI.